# Structural, magnetotransport, and optical properties of sputtered Co/Cu multilayers examined as a function of Co layer thickness at the second antiferromagnetic maximum

C. Christides[a)]
*Institute of Materials Science, NCSR ''DEMOKRITOS,'' 153 10 Agia Paraskevi Attiki, Greece*

S. Logothetidis, M. Gioti, and S. Stergioudis
*Solid State Physics Section, Physics Department, Aristotle University of Thessaloniki, 540 06 Thessaloniki, Greece*

S. Stavroyiannis and D. Niarchos
*Institute of Materials Science, NCSR ''DEMOKRITOS,'' 153 10 Agia Paraskevi, Attiki, Greece*

(Received 14 October 1997; accepted for publication 14 March 1998)

A series of $\{[\mathrm{Co}(t_{\mathrm{Co}})/\mathrm{Cu}(2.1\ \mathrm{nm})]_{30}/\mathrm{Co}(t_{\mathrm{Co}})\}_{30}$ multilayers have been deposited under specific magnetron sputtering deposition conditions that lead to giant magnetoresistance (GMR) curves with technological interest. X-ray reflectivity, magnetic, magneto-transport, and spectroscopic ellipsometry measurements were used together to examine the dependence of their properties upon the Co layer thickness ($t_{\mathrm{Co}}$). Remarkably, the obtained film density and roughness, the saturation and coercivity fields, the reduced remnant magnetization, the GMR ratios, and the plasma frequency exhibit a significant divergence as a function of $t_{\mathrm{Co}}$ in the range between 1.3–1.6 nm. The observed microstructural, magneto-transport, and magnetic *relative* differences, induced in (111) textured Co/Cu multilayers by varying the $t_{\mathrm{Co}}$, were correlated with changes of the optical electronic states of the constituents in the electronic density of states near the Fermi level. © *1998 American Institute of Physics.* [S0021-8979(98)02512-2]

## I. INTRODUCTION

Sputtered Co/Cu multilayers (MLs) with appropriate layer thicknesses exhibit giant magnetoresistance (GMR) ratios[1,2] up to 60% at room temperature in contrast to epitaxial MLs which register a much smaller GMR effect, and their magnetic switching field ($H_s$) is several times larger.[3] The observed GMR effect makes them potential candidates for magnetic sensor applications. However, to enable the potential of these magnetic sensors to be realized, large GMR ratios with low values of the $H_s$ should be developed.[4] Both the largest GMR and the lowest $H_s$ values were reported for films deposited by magnetron sputtering. Evidently some specific parameters of the developed microstructure reduce the coercivity, anisotropy, and magnetostatic coupling. Generally, in TM/NM MLs (TM=Fe, Co, Ni, or permalloy and NM=Cu, Ag, Au noble metals) the GMR ratio: $\mathrm{MR}_{\max}=(R_{\max}-R_s)/R_s$, with $R_{\max}$ and $R_s$ the maximum and minimum resistance as a function of the applied magnetic field $H$, respectively, are oscillating functions of spacer thickness ($t_{\mathrm{NM}}$) with maxima corresponding to an antiferromagnetic (AF) coupling between neighboring TM layers. It has been argued[5] that in sputtered Fe/Cu/Fe and Co/Cu/Co MLs the minority grains with (100) preferred orientation may be responsible for the AF interlayer coupling, while the dominant (111) textured grains account for their GMR. On the other hand, in Co/Cu(111) MLs grown by molecular beam epitaxy it is found[6] that the AF interlayer coupling at the first $\mathrm{MR}_{\max}$ peak is of an intrinsic nature and is not due to a small amount of misaligned crystallites with (100) texturing.

Besides their topological morphology, information about the electronic structure near the buried Co/Cu interfaces is valuable in order to understand the variation of magnetotransport properties as a function of $t_{\mathrm{Co}}$ or $t_{\mathrm{Cu}}$. It is well established by now[7] that the Co/Cu/Co trilayers exhibit an exchange coupling between the Co layers through the Cu spacer layer, which is an oscillating function of $t_{\mathrm{Cu}}$ with three well defined maxima. The Ruderman–Kittel–Kasuya–Yosida (RKKY) oscillations through the spacer, whose period depends on Fermi surface parameters, and the quantum-well spin-split states, whose occupation depends on their energy and hence on the layer thickness, are used to theoretically explain this behavior.[7] However, in epitaxial or polycrystalline TM/NM MLs, grown with a (111) preferred orientation, the observed[8,9] oscillatory interlayer exchange coupling is markedly different from the theoretically predicted $1/t_{\mathrm{Cu}}^2$ dependence. The magneto-optical Kerr effect and photoemission experiments were used extensively to obtain information about the interlayer magnetic coupling and the electronic states near the Fermi level. Optical studies in MLs with magnetic and nonmagnetic layers stacked alternately have shown[10,11] that, with the presence of interfaces, the interlayer interactions and the electronic structure of the individual layers induce well defined deviations of the dielectric function from that observed in single-layer films. Thus, varying the Co or Cu layer thickness is expected to affect the optical properties of the MLs by changing the roughness of Co/Cu interfaces and the grain sizes. Specifi-

a)Electronic mail: christides@ims.ariadne-t.gr

 

cally, the following changes in the MLs can vary the optical response function (dielectric function) of the films: (a) $3d$-spin polarization and $s$-$d$ hybridization effects near the Fermi surface of the constituents, (b) topological magnetostatic effects (dipole-field interactions), arising from roughness in the Co/Cu interfaces, that favor interlayer ferromagnetic (FM) coupling if the film growth is conformal and the magnetization is lying in the film plane,[12] (c) indirect exchange coupling that oscillates as a function of $t_{\mathrm{Cu}}$ between FM and AF coupling.[7]

Two different approaches have been reported in Co/Cu based structures that target low coercivity ($H_c$) and low switching ($H_s$) fields: either by forming MLs with $t_{\mathrm{Co}} \approx 1.5$ nm alternated with $t_{\mathrm{Co}} \approx 0.3$ nm layers[13] in the superlattice stacking: Co/Cu/Co/.../, or using spin-valve systems,[14,15] where a surfactant layer of In, Pb, or Au is introduced to control the long-wavelength (waviness) interface roughness. Recently a third way[16] has been demonstrated to control systematically the magnetostatic effects in sputter grown $[\mathrm{Co}(1\ \mathrm{nm})/\mathrm{Cu}(2.1\ \mathrm{nm})]_{30}$ MLs by selecting the surface substrate roughness and by using thermal isolation of the Si(100) substrate during magnetron sputtering with slow deposition rates of the constituents. The development of a specific microstructure, in terms of grain size and degree of layer texturing leading to macroscopic GMR parameters appropriate for use in active magnetic sensors, is achieved.[16] In the later approach is found that there is a bimodal distribution with two well separated populations of grain sizes below and above $\sim 12$ nm. It is observed that the growth of structures with average sizes less than 12 nm, with a volume fraction of $\sim 30\%$, increases the fraction of FM areas while it reduces the GMR ratio, the $H_c$ and $H_s$ values relative to samples with the same composition, consisting of grain sizes greater than 12 nm in a fraction of 90%. The reduction of GMR, $H_c$ and $H_s$ values, reported in Ref. 16, is due to a fraction of smaller grain sizes, that make the magnetostatic energy term important, whereas in Ref. 13 it is due to a decrease of magnetic anisotropy and magnetic moments in the Co layers. Thus, the developed micromagnetic state is completely different in the two categories of Co/Cu MLs, leading to different GMR and magnetic properties.

In the present study, the structural, magneto-transport, and optical properties of sputtered Co/Cu MLs are examined as a function of Co layer thickness at the second antiferromagnetic maximum. These MLs were grown under the specific deposition conditions, described in Ref. 16, that led to GMR curves with low hysteresis ($H_c$) and low switching ($H_s$) fields. Our particular aim is to connect the observed GMR curves with changes in the layering, surface morphology, and optical properties of these MLs. X-ray reflectivity (XRR) and spectroscopic ellipsometry (SE) were employed to investigate the structural characteristics as a function of $t_{\mathrm{Co}}$ in a series of $\{[\mathrm{Co}(t_{\mathrm{Co}})/\mathrm{Cu}(2.1\ \mathrm{nm})]_{30}/\mathrm{Co}(t_{\mathrm{Co}})\}$ MLs. The average density $\langle d \rangle$ and the Co/Cu interlayer and silicon nitride buffer layer rms roughness have been obtained from fits of the observed XRR spectra. In SE measurements a systematic variation of the real and imaginary parts $\epsilon_1(\omega)$ and $\epsilon_2(\omega)$ of the dielectric function has been observed as a function of Co layer thickness and the detected features were attributed to electronic structure effects of the Cu layers.

## II. EXPERIMENTAL DETAILS

Metallic disks of 99.99% pure elements with a diameter of 5 cm, were used as target materials in a high vacuum Edwards E360A sputtering system with a cluster of ATOM-TECH 320-SE planar magnetron sputter sources. The substrates were cut before deposition to a size of $1 \times 1\ \mathrm{cm}^2$. All samples were deposited in a cryogenically pumped chamber with a base pressure of $6 \times 10^{-7}$ Torr under an Ar (99.999% pure) pressure of 3 mTorr. During deposition the $\mathrm{Si}(100)/\mathrm{SiN}_x$ substrates were thermally isolated from the copper supporting table. An rf magnetron gun operating at 30 W with a deposition rate of 0.09 nm/s was used for Co, and dc sputtering at 5 W for Cu, resulting in a rate of 0.1 nm/s. Magnetic hysteresis loops were measured with a Quantum Design MPMSR2 superconducting quantum interference device (SQUID) magnetometer, positioning the sample with the magnetic field ($H$) direction lying in the film plane. MR measurements were performed with the four-point-probe method in samples with $0.4 \times 1\ \mathrm{cm}^2$ size, using a dc current of $I = 10$ mA. The field $H$ was lying in the film plane perpendicular to current flow direction. All measurements were performed at 300 K by first applying the maximum positive field $H$ parallel to the film plane and then completing the loop. The SE measurements were performed with a phase modulated spectroscopic ellipsometer, using a Xe lamp as light source for studies in the energy range 1.5–5.5 eV at a constant incidence angle of 70.4°, with a step of 20 meV. SE measurements allow the calculation[17] of the dielectric function $\epsilon(\omega) = \epsilon_1(\omega) + i\epsilon_2(\omega)$. The peak-to-peak surface roughness of the substrates has been estimated using the multi-mode atomic force microscope MMAFM-2/383, using the Nanoscope III SPM from Digital Instruments. AFM scans, performed on $1 \times 1\ \mu\mathrm{m}^2$ areas, gave rms values of surface roughness between 3 and 5 nm.

Six films of $\mathrm{Si}(100)\{\mathrm{SiN}_x(100\ \mathrm{nm})[\mathrm{Co}(t_{\mathrm{Co}})/\mathrm{Cu}(2.1\ \mathrm{nm})]_{30}/\mathrm{Co}(t_{\mathrm{Co}})\}$ MLs, with nominal $t_{\mathrm{Co}} = 0.6$, 0.9, 1.2, 1.6, 2.1, and 3 nm, were used. Their x-ray diffraction (XRD) spectra are characterized by an intense fcc (111) Co(Cu) peak and a weak (200) fcc peak, indicating that the MLs have strong (111) in-plane texture. The XRR measurements were performed with a Siemens D5000 reflectometer, using parabolic Göbel mirrors to increase intensity and make parallel the incident beam alignment of Cu $K_\alpha$ radiation. The setup can produce a parallel beam with a divergence less than 0.03° that allows analysis of films as thin as 2 nm. The $\theta$-$2\theta$ measurements were performed by using the same step of 0.006° in three ranges with the following settings: (i) for $2\theta = 0° - 0.66°$ at 0.1 kW x-ray tube power and 0.4 s/step; (ii) for $2\theta = 0.66° - 1.2°$ at 1.2 kW power and 2 s/step; and (iii) for $2\theta = 1.2° - 3.6°$ at 1.8 kW power and 5 s/step. The new hardware, used in this automated reflectometer, allows the placement of samples in the incident beam with a precision that guarantees that the absolute value of the incident angle can be reproduced within about 0.001°. Thus an accurate determination of the critical angle ($\theta_c$) value for total

reflection, that is directly related to the film density $d$ by $\theta_c \propto d^{1/2}$, can be achieved. Collimation of the incident beam is accomplished by a controllable knife edge over the sample. To estimate the experimental error introduced by curvature effects on the film surface, which is known to modify the reflectivity curves,[18] reflectivity measurements were performed by positioning every film in two different orientations rotated by 90° to each other. The adjustment of the apparatus has been performed by tracking the direct beam, which exhibits a Gaussian shape for the detected intensity, then setting in such that the grazing incident beam on the sample was found at the maximum of the Gaussian. At last, the tracking of the reflected beam is observed to exhibit a sharp Gaussian shape for the recorded intensity of the reflected beam, leading to unambiguous setting. Thus, the experimental reflectivity curves for the two different sample positions have shown the same fringe positions and intensities, with nearly the same plateau shape, for the total reflection area. Consequently, no serious curvature effects from the film surface were detected within our instrumental resolution. The REFSIM software, included in the Siemens D-5000 XRD, was used to fit the observed XRR data and the SIMPLEX algorithm was employed to perform the refinement with an optical model.

## III. OUTLINE OF THE PHYSICAL LIMITS IN THE OPTICAL MODEL USED FOR THE FITTING OF XRR SPECTRA

It is known[19,20] that the Fresnel reflectivity from MLs with perfectly flat interfaces, without a substrate, is composed from a type of $e^{iN\varphi}\sin N\varphi$ oscillation due to outer film interfaces plus a $e^{iN\varphi}\{[\sin(N-1)\varphi]/\sin\varphi\}$ term from the inner film superlattice units that produce the diffracted Bragg amplitude. The notation corresponds to: $\varphi=(2\pi/\lambda)n_f\Lambda\sin\theta$, with $\Lambda$ the bilayer thickness, $\theta$ the incident angle, $\lambda$ the x-ray wavelength, and $n_f$ an average refractive index for the film structure. Reflectivity spectra that measure the diffracted intensity of the MLs contain information on specular and diffuse scattering components along the specular direction from nonideal interfaces.[21] In MLs with correlated roughness, that is associated with conformal layer growth, consisting of $m$ different layers with layer thickness $t_i$ and density $d_i$ for every component, the rms roughness $\langle\sigma^2\rangle$ at each interface can be described by Gaussian statistics. In the optical model, if $D_i$ is the location of interface $i$ from the substrate ($D_i=\Sigma_{j=1}t_j$ and $D_o=0$) then the specular reflectivity $R(k_{z,0})$ decay as[20]

$$R(k_{z,0})=R_F(k_{z,0})\left[\sum_{i=0}^{m}\{(d_i-d_{i+1})/d_0\}\times\exp(-2ikD_i)\exp(-2k_ik_{i+1})\langle\sigma_{i+i}^2\rangle\right]^2, \quad (1)$$

where the subscript 0 indicates the air/specimen interface, $R_F$ is the ideal Fresnel reflectivity, and $k_i$ is the $z$ component of the wave-vector normal to film surface: $k=(2\pi/\lambda)\sin\theta$. For specular scattering the incidence and reflection angles are equal and consequently only the $k_z$ component is of interest. However, in diffuse (nonspecular) scattering these angles are not equal and lead to nonzero $k=(k_x,k_y,k_z)$ components that contribute to extra scattering along the specular direction $k_z$ as well. Thus, a correlation length $\xi$ of roughness, that refers to the lateral distance along an interface at which the $z$ heights of two points on the surface become statistically uncorrelated, should be taken into account for the correct calculation of the XRR spectra. The change caused by these factors in the specular reflection coefficient $r(k,0)$ for a single layer $[R(k,0)=r(k,0)r^*(k,0)]$ is approximated by[22]

$$r(k,0)\approx r_F(k,0)\exp[-2k_0k_1\langle\sigma^2\rangle - 1/(2\pi^2)k_0k^2(1-n_1^2)C(\xi)], \quad (2)$$

where $C(\xi)$ is the correlation function of roughness, which decays like $C\langle\sigma^2\rangle e^{-x/\xi}$, whereas $C=1$ for total correlation, $C=0$ for no-correlation, and $0<C<1$ for partially correlated interfaces. Furthermore, $k_0$ is the incident wave vector, $k_1$ is the transmitted component in the film, and $n_1$ is the refractive index of the film. For $C=1$ the rms interface roughness $\langle\sigma_o^2\rangle$ is the same for all layers. If $\xi\ll k/k_0^2$ then Eq. (2) becomes: $r(k,0)\approx r_F(k,0)\exp(-2k_0k_1\langle\sigma_o^2\rangle)$, that is the derived formula by Nevot and Croce in the limit of high spatial frequency ($\sim$nm) roughness.[23] If $\xi\gg k/k_0^2$ then Eq. (2) becomes $r(k,0)\approx r_F(k,0)\exp(-2k_0^2\langle\sigma_o^2\rangle)$, that has the form of a Debye–Waller factor in the limit of low spatial frequency or long-wavelength ($\sim\mu$m) waviness. For $C=0$ the rms roughness $\langle\sigma_i^2\rangle$ is different for every interface $i$ and for $0<C<1$ both $C_i$ and $\langle\sigma_i^2\rangle$ vary from top to the bottom of the MLs. Thus, when the layer morphology in a multilayered structure deviates from the $C=1$ and $\xi\gg k/k_0^2$ conditions, then refinement of the observed spectra with the REFSIM routine, that uses an optical model where a common Debye–Waller factor is assumed for all layers of the same component, leads to underestimated or overestimated $d_i$ and $\langle\sigma_0^2\rangle$ values.

Since bulk Co and Cu have similar densities ($\sim$8.9 g/cm$^3$), Eq. (1) indicates that Co/Cu MLs will exhibit small x-ray contrast because the amplitude of fringes in a reflectivity profile depends upon the reflectivity contrast at interlayer interfaces. However, when Cu $K\alpha$ radiation is used the Fresnel coefficient at Co/Cu interfaces is dominated by the difference in the imaginary parts of the refractive indices[19] and leads to asymmetric superlattice reflections depending whether the x-ray beam encounters the structure Co/Cu/Co/Cu... or its mirror image. In the multilayers examined here, the layer stacking is symmetric to Co on top and bottom of the film and the asymmetry around the first Bragg peak is reduced. Thus, the major contribution in the observed reflectivity profiles is expected from x-ray contrast and roughness of the outer interfaces, which we define as the air film and film substrate correspondingly.

## IV. EXPERIMENTAL RESULTS

### A. Refinement of XRR data

The observed spectra are plotted with a 5% offset relative to the best obtained fitting curves in Fig. 1. Several assumptions concerning: (i) the air-film interface on top of

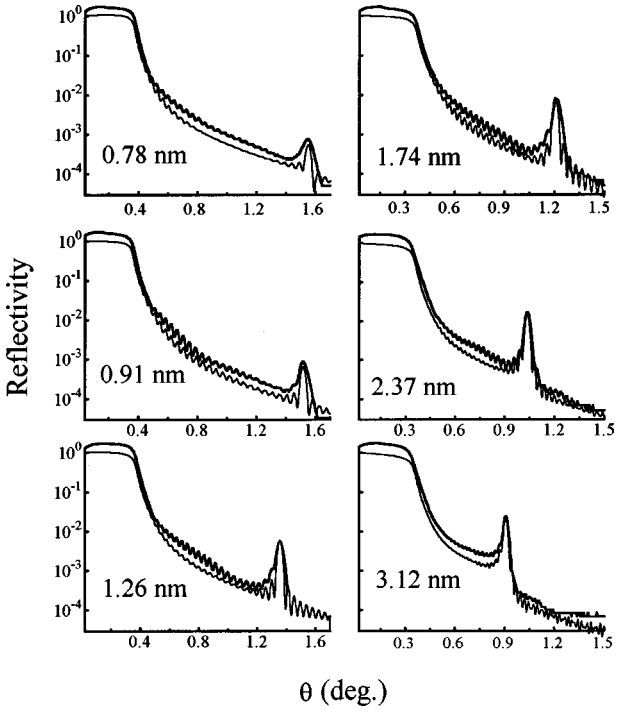


FIG. 1. X-ray reflectivity profiles of Si(100)/{$SiN_x$(100 nm)/{[Co($t_{Co}$)/Cu(2.1 nm)]$_{30}$/Co($t_{Co}$)} MLs with nominal $t_{Co}=0.6$, 0.9, 1.2, 1.6, 2.1, and 3 nm. The observed spectra are plotted with a 5% offset (thick line) over the calculated profiles for clarity. The refined Co layer thicknesses ($t_{Co}$) are displayed in every spectrum.

film, (ii) the interlayer interfaces inside the film, and (iii) the substrate-film interface, were made in order to account for the observed: (a) reduced amplitude in Kiessig fringes and (b) the broad Bragg peaks from the $N=30$ superlattice periods. The REFSIM software allows the fitting of thickness $t_i$, rms roughness $\langle\sigma^2\rangle$, and density $d$ for groups or individual adjacent layers. Since a reliable refinement of MLs requires the smallest possible number of variable layer parameters, we used a group of N bilayers with the common three mentioned variables for every component for the fitting. In order to derive a model that may better describe the observed profiles, four separated fitting steps were employed:

(a) First, a group of $N=30$ Co/Cu bilayers with only six variable parameters, three for every component, is considered. The 100 nm thick $SiN_x$ buffer layer was included in the calculation, using a fixed rms roughness of 0.6 nm and a fixed $d(SiN_x)=2.3$ g/cm$^3$ parameter. The calculated reflectivity spectrum gave a first estimation of $t_{Cu}$, $t_{Co}$ and $\langle d\rangle$ parameters. A systematic decrease of $\langle d\rangle$, from 7.1 to 6.2 g/cm$^3$, has been found with increasing $t_{Co}$. However, the estimated amplitude and decay slope of the reflectivity oscillations were very different (about 50%) from the observed spectra.

(b) To take into account the effect of extended rms roughness in Co/Cu interfaces, a third CoCu interlayer has been introduced for every bilayer making a group of $N=30$ trilayers with nine variable and properly adjusted parameters. Only a slight improvement is achieved relative to the previous model, concerning the amplitude of the undulations, while the calculated spectra were still different from those observed.

(c) Since the range of estimated $\langle d\rangle$ values was found to be much lower than the 8.9 g/cm$^3$ bulk value, a considerable contribution from layer waviness is probable. Thus, a third attempt was to keep the $N=29$ bilayers of the first model and allow the parameters of the Co cover layer, plus the next two Cu and Co layers on top, to vary independently from the group parameters. In this way the effect from film surface waviness is taken into account. This time a better agreement has been achieved between the calculated and observed decay slope of reflected intensity but the estimated amplitude of the undulations remained large. Remarkably, the variation of $\langle d\rangle$ values with $t_{Co}$ has been changed drastically for the group of $N=29$ bilayers. Thus values of $\langle d\rangle$ ranging between 7.1 and 8.7 g/cm$^3$ were found. This happened because the $d$ parameter of the Co cover layer was lowered to $\sim 5.8(\pm 0.2)$ g/cm$^3$ while its $\langle\sigma^2\rangle$ parameter was always converged to very low values ($\sim 0.1$ nm). Top layer oxidation and film surface waviness can be related to this result.

(d) Finally, the effect of film-substrate roughness is included in the refinement. Thus, the third model was modified by considering from top to bottom of the film a variable Co cover layer followed by a group of $N=29$ bilayers plus two Cu and Co layers adjacent on a $SiN_x$ buffer layer with variable parameters. After an extensive search in the parameter space the refinement was converged to meaningful physical values when: (1) only the Co cover layer parameters were varied during the fitting while all the other parameters were fixed for the Co/Cu multilayer, (2) then only the film-$SiN_x$ parameters were fitted, and (3) only the six parameters of the Co/Cu group, with $N=29$ bilayers, were allowed to vary during fitting. The best fitted spectra are shown in Fig. 1. In Fig. 2 the estimated Co/Cu film density $\langle d\rangle$ (top), the rms roughness in the film-substrate interface (middle), and the rms roughness $\langle\sigma^2\rangle$ of Co layers in the multilayer (bottom) as a function of the obtained $t_{Co}$ values, are plotted. The agreement between observed and calculated spectra (Fig. 1) indicates that the film surface waviness and the film-substrate interface roughness affect predominantly the x-ray reflectivity in this series of Co/Cu MLs. The obtained $t_{Co}$ values are given in Fig. 1. The $t_{Cu}$ values were estimated at about $2.1(\pm 0.3)$ nm for all the MLs. A satisfactory agreement is found between nominal and estimated $t_{Co}$ and $t_{Cu}$ values. However, in the MLs with nominal $t_{Co}=0.6$ nm a 30% deviation is obtained from the estimated value of 0.78 nm. Since this is the thinner Co/Cu multilayer, with a total film thickness of $\sim 88$ nm, the x-ray beam penetrates the $SiN_x$ buffer layer. Consequently, a statistical error is introduced from reflectivity contrast in the film-substrate interface and from some degree of Co–Cu intermixing that causes the observed deviation in $t_{Co}$ value. In summary, the fitting of XRR spectra with an optical model gave the following results:

(i) The $\langle d\rangle=8.6$ g/cm$^3$ value for the MLs with $t_{Co}\sim 0.78$ nm is close to 8.9 g/cm$^3$ that is expected for a thick Co or Cu film, while for all the other MLs $\langle d\rangle$ falls in the range of 7.1–7.7 g/cm$^3$. It is well known[20] that the measured reflectivity is a result of the variation in the scattering length

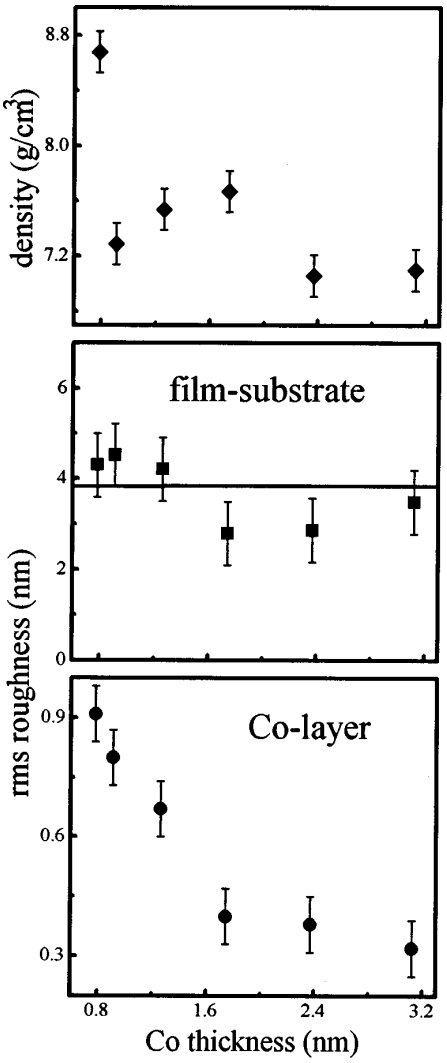


FIG. 2. The estimated Co/Cu film density $\langle d \rangle$ (top), the rms roughness of the film-substrate interface (middle), and the rms roughness $\langle \sigma^2 \rangle$ of Co in Co/Cu interfaces (bottom) are plotted as a function of the estimated $t_{Co}$ from the XRR data analysis.

(proportional to electron density) projected onto a ray normal to the surface. In this experiment the coherence length, over which the electron density is projected onto surface normal, is estimated to be $\sim 10\ \mu$m at an incidence angle of 0.3° and is a macroscopic distance. Thus, the obtained drop of $\langle d \rangle$ (Fig. 2) can be associated with film surface roughness that creates a density gradient for $t_{Co} > 0.8$ nm. Our results indicate that the surface roughness of Co/Cu MLs can be modified when nucleation of pure Co seeds occurs for thicker Co layers. This can be realized by considering columnar growth of Co/Cu crystallites with a bimodal distribution of grain sizes[16] that produces a pronounced surface roughness on top of the film for thicker $t_{Co}$, in analogy to formation of quantum dots on the surface of GaAs/$Ga_{17}In(Al)_xAs$ strained superlattices grown in the Stranski-Krastanow mode. Accordingly, scanning tunneling microscopy[24] and X-ray absorption spectroscopy[25] measurements performed in sputtered Co/Cu MLs show an island-upon-island layer growth that is conformal from layer to layer and leads to pyramidal structures. Also, scanning tunneling microscopy measurements[24] performed on the surface of a $[\mathrm{Co}(2.1\ \mathrm{nm})/\mathrm{Cu}(2.1\ \mathrm{nm})]_5$ film covered with a Co layer, 2.1 nm thick, reveal a vertical surface roughness of $\sim 10$ atomic steps and a terrace width of $\sim 2$ nm. Thus, the effect of pyramidal growth in Co layers is enhanced by increasing $t_{Co}$ and creates larger surface anomalies between the grain boundaries of columnar crystallites with small and large sizes. Such surface modification may well account[20] for $\langle d \rangle$ value deviations in XRR measurements.

(ii) A high rms roughness in the film/$SiN_x$ interface is found to induce the damping of the reflectivity fringes in the calculated spectra, while for the $SiN_x$ buffer layer the $\langle d \rangle$ value is estimated at about $2.4(\pm 0.04)$ g/cm$^3$ that is close to the bulk value.[20] However, the obtained $\langle \sigma^2 \rangle$ values for the film/$SiN_x$ interface is in agreement with the rms roughness observed from AFM measurements of the substrate surface (Sec. II). Consequently, the $\langle \sigma^2 \rangle$ values in Fig. 2 express the average amplitude of film/substrate waviness that is induced by the substrate surface roughness.

(iii) The decrease of $\langle \sigma^2 \rangle$ values in the Co layers by increasing $t_{Co}$ may signify the formation of relaxed Co atomic planes[26] for $t_{Co} > 1.6$ nm. The observed superlattice Bragg peak indicates that chemical intermixing does not dissolve the bilayer stacking for the thinner $t_{Co}$. Since for $t_{Co} < 1.6$ nm the $\langle \sigma^2 \rangle$ values increase and become comparable to $t_{Co}(\sim 0.8$ nm) for the thinnest MLs, it is reasonable to assume that the island-upon-island growth mode is enhanced, leading to conformal layering of Cu on Co. This kind of growth mode creates an interface roughness with high spatial frequency that might be approximated by the Nevot and Croce formula (see Sec. III). Since the REFSIM routine uses a Debye–Waller factor, the increase of $\langle \sigma^2 \rangle$ values for $t_{Co} < 1.6$ nm gives the composition limit where the Co layering changes. However, the quantitative estimation of $\langle \sigma^2 \rangle$ becomes marginable. For $t_{Co} > 1.6$ nm the lattice relaxation of the inner Co atomic planes alter the Co on Cu growth process and leads to nonconformal interface roughness, that is characterized by large lateral length scales or long-wavelength layer waviness. This kind of spatial roughness is better approximated by the Debye–Waller factor. Thus, for $t_{Co} > 1.6$ nm the obtained $\langle \sigma^2 \rangle$ values of 0.4 nm approach the range of rms interface roughness that is usually obtained in metallic MLs.

### B. Effect of $t_{Co}$ on the magnetic and magnetotransport properties

In Fig. 3 are shown the observed GMR and reduced magnetization $M/M_s$ vs $H$ hysteresis loops for the $\{[\mathrm{Co}(t_{Co})/\mathrm{Cu}(2.1\ \mathrm{nm})]_{30}/\mathrm{Co}(2.1\ \mathrm{nm})\}$ MLs, with $M_s$ the magnetization measured at 10 kOe. The observed parameters $(\Delta R/R)_{max}$, $H_s^R$, $H_c^R$, that are extracted from the GMR loops, and the $M_r/M_s, H_s^M, H_c^M$ values, obtained from the corresponding magnetic loops, are plotted in Fig. 4 as a function of $t_{Co}$. The notation corresponds to: $M_r$ the remnant magnetization for $H=0$; $H_s^R(H_s^M)$ is the switching (saturation) field where the film resistivity (magnetization) approaches the lowest (maximum) value; and $H_c^R(H_c^M)$ is the

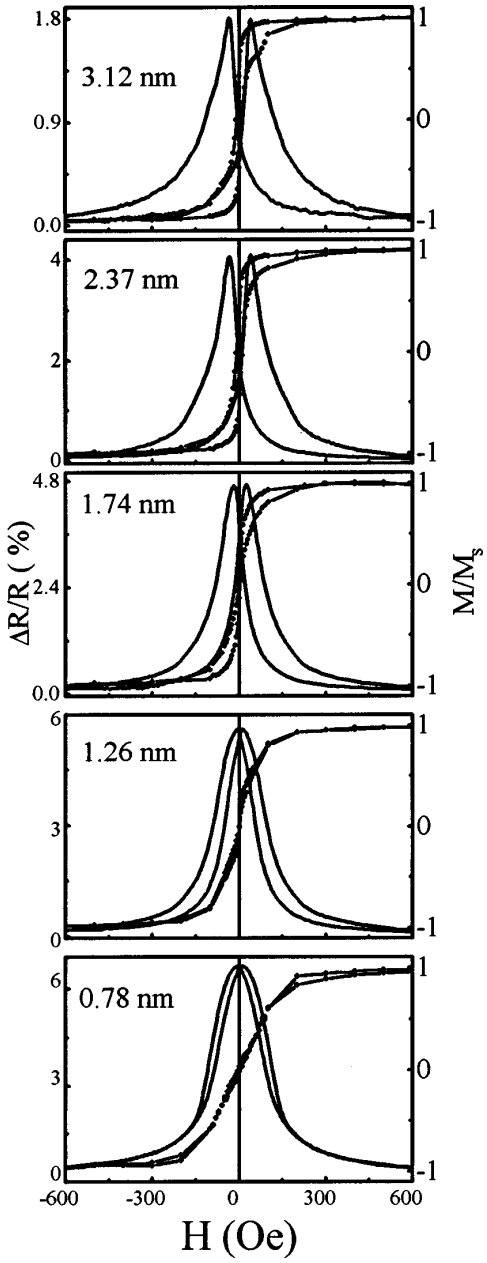


FIG. 3. The observed GMR (left-hand axis) and reduced magnetization hysteresis loops (right-hand axis) are shown as a function of $t_{Co}$.

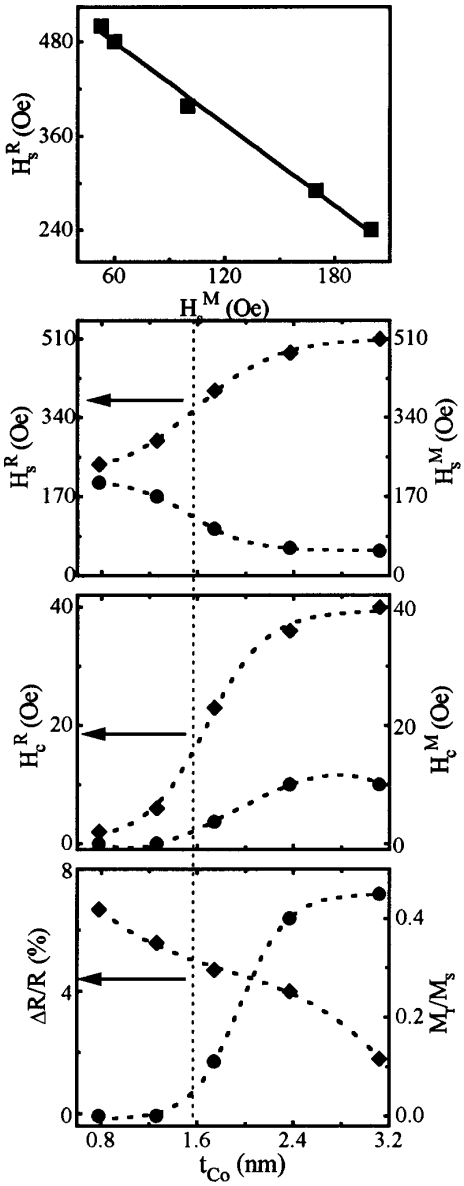


FIG. 4. The observed parameters: $\Delta R/R$, $H_c^R$, $H_s^R$ (left-hand axis), and $M_r/M_s$, $H_c^M$, $H_s^M$ (solid circles), are plotted as a function of $t_{Co}$. The plot on top shows the linear variation of $H_s^R$ with $H_s^M$. A detailed explanation of the parameters is given in the text. The dotted lines are used as guides to the eye while the vertical dashed line indicates a boundary between the intermediate and long-$\Lambda$ regime (see Sec. IV C).

coercive field where the film resistivity (magnetization) exhibits its maximum (zero) value. Since there are long tails in the GMR and magnetization curves (Fig. 3) the $H_s$ values were selected at points where the first derivative $d(\Delta R/R)/dH$ equals 0.01 and the $M/M_s \approx 0.93(\pm 0.03)$, respectively. Obviously, a decrease of $H_c$ and $H_s$ values is observed from magnetic and magneto-transport properties when $t_{Co} < 1.6$ nm while the obtained GMR curves suggest that MLs with $t_{Co} \leqslant 1$ nm can be used for sensor applications. However, for $t_{Co} \leqslant 0.5$ nm we have found a drop of GMR ratio down to 3% which imposes a bottom limit in $t_{Co}$ for the specific Co/Cu MLs. In addition, Fig. 4 shows three characteristic features which are indicative of a peculiar behavior in these Co/Cu(111) MLs. These are:

(i) A decrease of the $\Delta R/R$ ratio as a function of $t_{Co}$ [Fig. 4 (bottom)], that is different from the $\Delta R/R$ vs $t_{Co}$ variation[26] observed in Co/Cu MLs grown on 5 nm Fe buffer layer, where the dominant contribution in the GMR effect arises from spin-dependent scattering at interfaces.

(ii) The variation of $M_r/M_s$, $H_c^M$ and $H_c^R$ values with $t_{Co}$ exhibit an abrupt increase for $t_{Co} > 1.3$ nm. This may imply an enhancement of FM coupled film regions and a hardening in the magnetization reversal of the magnetic domains for $t_{Co} > 1.3$ nm. Since coercivity is associated with an anisotropy field $H_A = 2K_{eff}/M_s$, where $K_{eff}$ is the effective anisotropy per unit volume for FM coupled Co layers, then its Co thickness dependence is usually connected with variations of the macroscopic interface ($K_S$) and volume ($K_V$) magnetic anisotropy components.[27,28] These are related by

the phenomenological expression: $K_{\text{eff}}=K_V+2K_S/t_{\text{Co}}$. If $K_S$ and $K_V$ are constants then a linear plot of $K_{\text{eff}}t_{\text{Co}}$ against $t_{\text{Co}}$ gives an intercept at $2K_S$ for $t_{\text{Co}}=0$ and a crossover to perpendicular anisotropy occurs ($K_{\text{eff}}=0$) at the critical Co layer thickness of $-2K_S/K_V$. However, this treatment is found unsatisfactory since it does not reproduce the behavior at small $t_{\text{Co}}$ values where a deviation of $K_{\text{eff}}$ is often observed,[29] as in our case. For coherent MLs the $K_V$ term contains[27] contributions from shape, magnetocrystalline (MC), and various forms of strain anisotropy while interface anisotropy is solely due to Néel surface anisotropy.[29] In the incoherent case, misfit strain anisotropy may also contribute to $K_S$. Thus, in Co/Cu(111) superlattices, where the adjacent Co and Cu layers occur with the same in-plane lattice parameter (coherent) without misfit dislocations at the interfaces up to large layer thicknesses, the Co layer anisotropy has been described adequately[29] by replacing $K_S$ with a thickness-dependent magnetoelastic anisotropy term. This model describes a gradual approach of $K_{\text{eff}}t_{\text{Co}}$ to zero for $t_{\text{Co}}<2$ nm, that is observed in Co($t_{\text{Co}}$)/Cu(2.5 nm) superlattices[28] where the Co layers are FM coupled, by introducing a significant reduction of the Co MC anisotropy and entering the interfaces only as the source of an epitaxial strain which exist throughout the entire Co layer. In our case, the abrupt reduction of $H_c$ parameters for $t_{\text{Co}}<2$ nm, observed in Fig. 4 (middle), coincides with a reduction of the remnant magnetization $M_r/M_s$ ratio and enhancement of the GMR. This observation that the increase in the GMR was always accompanied by a decrease of the $M_r/M_s$ ratio was also found in other Co/Cu and Fe/Cr MLs[30] and was related with an enhancement in the fraction of AF exchange coupled Co layers. In GMR superlattices or polycrystalline MLs, with grain sizes larger than the mean-free electron path (that is 20–25 nm in transition metals), the observed increase of GMR ratio by decreasing $t_{\text{Co}}$ can be understood with a balance[30c] between the indirect exchange coupling energy $J_{\text{AF}}$ and the $K_{\text{eff}}$ as a function of $t_{\text{Co}}$. However, in our Co/Cu MLs there is a significant magnetostatic energy term $E_m \propto M_s$, arising mainly from the grain boundaries of columnar crystallites with sizes less than 12 nm, that overcomes the $J_{\text{AF}}$ and $K_{\text{eff}}$ terms by increasing $t_{\text{Co}}$. It was observed[16] that a 30% fraction of small crystallites reduces the GMR ratio down to 6%, from the 16% observed[16] when their fraction becomes less than 10%, and were associated directly with an increase of the $M_r/M_s$. Therefore, any increase of the $M_r/M_s$ from zero can be associated with a parallel alignment of magnetic components that appear as a FM contribution in the hysteresis loops. The dipole fields, induced from structural Co/Cu interface anomalies and the $E_m$ from the grain boundaries, interact in a manner that tends to produce parallel alignment of magnetic moments[12] between adjacent Co layers for $t_{\text{Co}}>1.6$ nm. Since $M_s$ decreases rapidly by decreasing $t_{\text{Co}}$ below 3 nm, then $E_m$ becomes smaller than the $J_{\text{AF}}$ and $K_{\text{eff}}$ terms below a critical $t_{\text{Co}}$ and causes the observed variations in the range 1 nm$<t_{\text{Co}}<2$ nm. Consequently, the observed changes for $t_{\text{Co}}<2$ nm can be related with the layer morphology that is developed in Co as a function of $t_{\text{Co}}$.

(iii) A deviation is observed between the $H_s^R$ and $H_s^M$ parameters (Fig. 4), with $H_s^R$ ascending and $H_s^M$ descending by increasing $t_{\text{Co}}$, while both approach an upper and a lower limit, respectively, for $t_{\text{Co}}>2$ nm. This behavior can be explained by the gradual approach to saturation in the GMR curves that is associated with curling details of the magnetization near the film edges[31] and is a characteristic of the specific stripes with $0.4\times 1$ cm$^2$ size. This effect can be associated with the linear correlation: $H_s^R \approx -\sqrt{3}H_s^M$, that is shown in Fig. 4 (top). The large divergence of $H_s^R$ and $H_s^M$ values demonstrate the ability of film size and shape effects to modify the extrinsic magnetic properties of Co/Cu MLs when the Co layer magnetization and anisotropy vary by increasing $t_{\text{Co}}$.

In summary, the observed magnetic loops indicate that the magnetic configuration evolves from a state where a large fraction of AF coupled Co/Cu regions coexist with a small fraction of FM coupled areas for $t_{\text{Co}}<1.6$ nm, to a micromagnetic state where the FM fraction becomes dominant by increasing $t_{\text{Co}}$. This effect can be related to the layering and surface morphology of the MLs. Generally, it is accepted that for conformal growth of columnar grains the interlayer Co exchange coupling is AF for the proper $t_{\text{Cu}}$ because the RKKY interactions are preserved. However, the obtained XRR results indicate that the Co/Cu multilayer structure deviates from conformal growth for $t_{\text{Co}}>1.6$ nm. In agreement, it is reported[32] that for sputtered Co/Cu MLs with (111) texturing, the layer stacking may alternately roughened by Co on Cu growth and smoothened by Cu on Co growth in a way that results in nonconformal growth for the thicker Co layers. Thus, the deposition of Cu may smooth the underlying Co layer waviness in a way that the RKKY interaction is effectively averaged out by local variations of $t_{\text{Cu}}$ in Co/Cu MLs with $t_{\text{Co}}>1.6$ nm. Consequently for $t_{\text{Co}}>1.6$ nm, where FM coupled areas are dominant, the observed low GMR ratio might be caused by the small residual fraction of the remaining AF aligned regions.

### C. Dielectric function variation determined from SE

Since SE in metallic MLs has only been used very recently, the information that is contained in the collected spectra must be specified for every case. Thus, a comprehensive understanding of our data can be made by explaining the involved optical properties in SE for the constituents (Cu and Co) of the MLs. The SE measurements concern observations of the complex reflection ratio: $\rho=\tan\psi e^{i\Delta}$. By using the measured ellipsometric angles $(\psi,\Delta)$ corrected pseudo-dielectric functions $\epsilon(\omega)=\epsilon_1(\omega)+i\epsilon_2(\omega)$ are calculated from the complex reflectance ratios. In general, these optical properties are correlated to the electronic properties of a material. If the solid is a good conductor, like metals, the optical wave interacts mainly with conduction electrons and, according to the Drude theory,[33] the plasma frequency $\omega_p$ of the electron gas plays the most important role. Consequently, there is a characteristic $1/\omega^2$ free-electron behavior in the variation of $\epsilon(\omega)$ with the photon energy $\omega$. However, the measured absorption ($\epsilon_2$) in bulk Cu[34] shows a sharp increase at about 2 eV and its reddish color is a manifestation of the rather low threshold for the excitation of $3d$-band

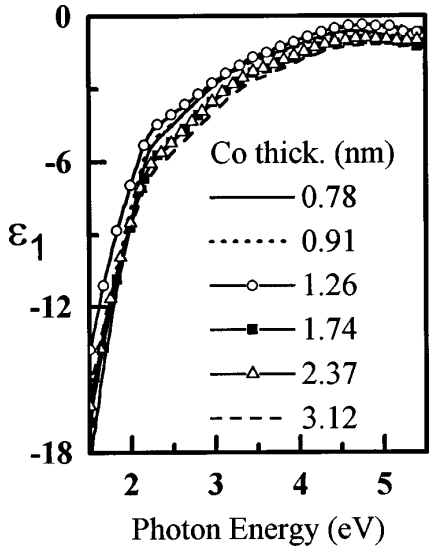


FIG. 5. The obtained real part $\epsilon_1$ of the dielectric function is plotted as a function of the photon energy for the six Co/Cu multilayers with different $t_{Co}$.

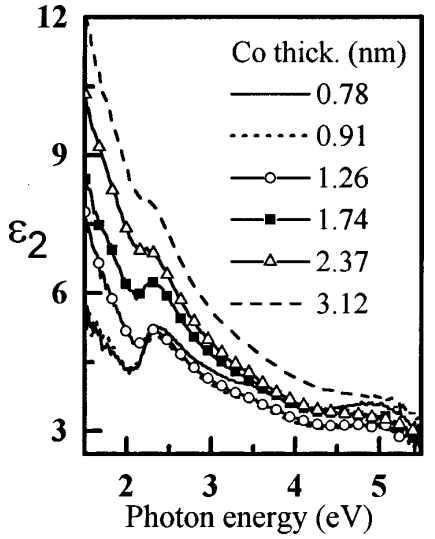


FIG. 6. The obtained imaginary part $\epsilon_2$ of the dielectric function is plotted as a function of the photon energy for the six Co/Cu multilayers with different $t_{Co}$.

electrons in the conduction band. On the contrary, the optical reflectance of pure Co films[35] is low and decreases smoothly, but in a very different way to that expected from a ''free-electron'' metal, while its $\epsilon_2(\omega)$ curve exhibits a slight structure near 5.5 eV. Also, it is found that formation of a surface CoO layer on Co films shifts only the reflectance curves without changing their shapes.[34] Finally, the striking similarity observed[36] in the optical density of states of pure Ni(fcc), Co(hcp), and Fe(bcc) films suggests that the crystal symmetry does not have a first-order effect on them. Since $\epsilon_2$ is proportional to the real (absorptive) part of the conductivity, that is of interest in the present study, the SE spectra obtained here are discussed only in view of these terms. The obtained $\epsilon_1(\omega)$ and $\epsilon_2(\omega)$ spectra are plotted in Figs. 5 and 6. These spectra exhibit three characteristic features that generally appear in metallic multilayers of Cu and are well explained from their common electronic and structural modifications:

(a) Both the real and imaginary parts of $\epsilon(\omega)$ show a monotonic, systematic shift with increasing $t_{Co}$, moving from Cu-like optical constants to Co-like constants.[11]
(b) The $\epsilon_1(\omega)$ and $\epsilon_2(\omega)$ spectra exhibit a well defined interband peak at $\sim 2.2$ eV and a second broad feature at about 4.8 eV, that are similar to those observed in Cu/Ni[10] and Cu/Co[11] MLs.
(c) The large interband peak broadening that is observed in Cu based MLs, compared to the sharp threshold absorption edge of bulk Cu,[33] is due to symmetry breaking at the interfaces of the multilayer and the confinement of the electronic mean-free path from grain boundaries.

Our aim is to explain the *relative* differences between the observed $\epsilon(\omega)$ spectra by considering only the changes in the optical electronic states as a function of $t_{Co}$. Therefore, a quantitative estimation of the involved spectral parameters is required. A reasonable analysis of the observed interband transition peaks can be approximated with standard analytical line shapes.[33] However, the selection of the appropriate $\epsilon(\omega)$ fitting function requires a tentative assignment of these two features to the band structure critical points for the Co and Cu layers.[17] It is well known that the $\epsilon_2(\omega)$ optical spectrum of pure Cu[33,34] exhibits two characteristic peaks at about 2 and 5 eV. The peak near 2 eV is assigned to transitions between the uppermost, nearly flat, $3d$ valence band and an $s,p$-like conduction band just above the Fermi level. The three independent components of the strain optical tensor:[33,37] $W_{11}+2W_{12}$, $W_{44}$, and $W_{11}-W_{12}$, obtained from the piezoreflectance spectrum of single crystal Cu, illustrate the fact that the 2 eV transitions do not occur exactly at $L$ high symmetry point but in a rather low symmetry region ($W$-$L$ line) of **k** space. According to empirical band calculations, the peak position near 5 eV may occur from transitions corresponding to different critical point in the first Brilluin zone of Cu. The first assignment[33] is made to an $M_1$ critical point at $X(X_5 \rightarrow X_{4'})$. The second assignment is made to a sum of two contributions:[34] one due to transitions from the lowest lying $3d$ states (band 1) into the $s,p$ band (band 6) and the other between the $s,p$-like states from bands 6–7 across the gap $L_1-L_{2'}$. The $X$ and $L$ high symmetry points belong to the faces where the $\langle 100 \rangle$ and $\langle 111 \rangle$ cubic directions, respectively, intersect the first fcc Brillouin zone. Thus, if there is such preferential orientation across the growth direction of the MLs, an additional broadening can be induced at the 5 eV peak from the Co/Cu interfaces. Since the examined Co/Cu MLs exhibit some degree of (111) texturing and the Co layers have an fcc atoming packing, the observed differences among the $\epsilon(\omega)$ spectra can be related to hybridization of Cu energy levels that is induced from adjacent Co sites at the Co/Cu interfaces. In this way, unoccupied free-electron like bands of pure Cu, lying above and near the Fermi level, can be intermixed[11] with unfilled Co $3d$

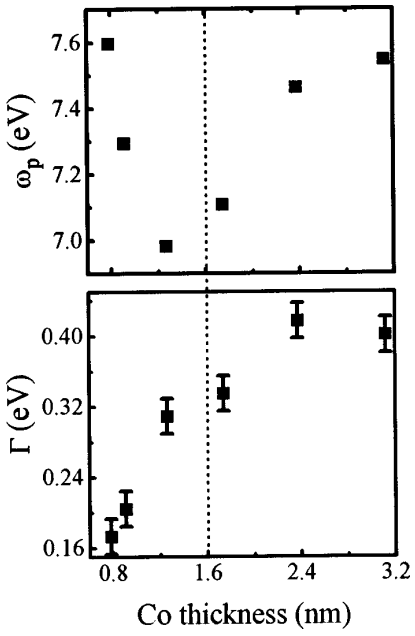


FIG. 7. The estimated values of the plasma energy $\omega_p$ (top) and the broadening parameter $\Gamma$ (bottom), from Eq. (3), are plotted as a function of the estimated $t_{\mathrm{Co}}$ values from the XRR data analysis. The vertical dashed line indicates a boundary between the intermediate and long-$\Lambda$ regime (see Sec. IV C).

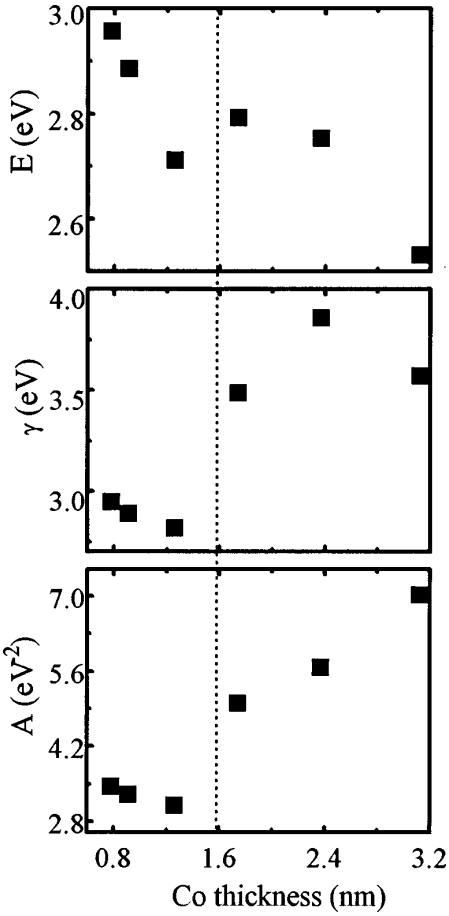


FIG. 8. The estimated values of the interband peak energy position $E$ (top), the broadening parameter $\gamma$ (middle), and amplitude $A$ parameter (bottom), from Eq. (3), are plotted as a function of the estimated $t_{\mathrm{Co}}$ values from the XRR data analysis. The vertical dashed line indicates a boundary between the intermediate and long-$\Lambda$ regime (see Sec. IV C).

states. This will cause a shift of the absorption peak positions and create a distribution of nearby band transitions that can smear out the threshold energy.

A phenomenological expression, that takes into account the free-carrier and photon absorption from intra-band and interband electron transitions, is used for the fitting of the dielectric function. The $\epsilon(\omega)$ fitting function is written[38] as the sum of a Drude term plus a damped Lorentzian oscillator term, centered at the low energy interband peak position $(h\omega_0/2\pi)$ with a strength $A$ and a damping (broadening) factor $\gamma$. A second Lorentzian term is used for the feature near 5 eV in order to take into account the vast peak broadening that extends beyond the recorded spectral limits. The analytical expression contains a constant background term $\epsilon_\infty$ as well

$$\epsilon(\omega)=\epsilon_\infty-\frac{\omega_p^2}{\omega(\omega+i\Gamma)}+\frac{A}{\omega_0^2-\omega^2-i\gamma\omega}. \tag{3}$$

In the second (Drude) term $\omega_p=(4\pi N_c e^2/m^*)^{1/2}$ is the unscreened plasma energy related to the density $N_c$ of the free carriers with $m^*$ being the effective mass and $\Gamma(\sim 1/\tau)$ being the broadening parameter, which is inversely proportional to the free-carrier's scattering time $\tau$. A quantitative estimation of $\omega_p$, $\Gamma$, of the energy peak position, the amplitude—that depends upon the strength factor $A$—and the broadening $\gamma$ parameters is achieved by simultaneous least-square fitting of the real and imaginary parts of the $\epsilon(\omega)$ spectra. The obtained plasma energy $\omega_p$ (top) and broadening $\Gamma$ (bottom) parameters are plotted in Fig. 7 against $t_{\mathrm{Co}}$. In Fig. 8 the interband peak transition energy $E$ (top), the damping oscillator factor $\gamma$ (middle), and the weighting strength factor $A$ (bottom) are plotted as a function of $t_{\mathrm{Co}}$. Both plots exhibit a nonmonotonic variation of the intra-band and interband parameters with $t_{\mathrm{Co}}$ and show a different dependence upon the modulation period $\Lambda=t_{\mathrm{Co}}+t_{\mathrm{Cu}}$ for $t_{\mathrm{Co}}>1.3$ nm. However, the phenomenological description of the interband parameters $E=h\omega_0/2\pi$ and $\gamma$ [Eq. (3)] does not allow their interpretation as absolute values that can be compared with calculated band structure transitions. These parameters are only indicative of the relative trend that is followed as a function of $t_{\mathrm{Co}}$. The possible physical origin of the observed trend in Figs. 7 and 8 is discussed below.

First, the variation of the obtained intra-band parameters is compared to those reported for other metallic MLs. Figure 7 (top) shows the plasma energy $\omega_p$ to decrease for $t_{\mathrm{Co}}<1.3\,nm$, whereas an increase is observed for $t_{\mathrm{Co}}>1.3$ nm. Remarkably, this variation of $\omega_p$ with $t_{\mathrm{Co}}$ is inverse to that obtained in Pd/Ni MLs[38] with $t_{\mathrm{Pd}}$ or $\Lambda=t_{\mathrm{Pd}}+t_{\mathrm{Ni}}$. It is reasonable to relate this behavior to a common modification in the layering of the two systems by changing $\Lambda$. In a first approximation, the structural modulation of the MLs is caused by the strain energy due to the lattice mismatch along the (111) direction. This mismatch is about 2% in Co/Cu MLs and about 10% in Pd/Ni MLs. A comparative study of Cu/Ni and Pd/Ni MLs,[39] that exhibits the same difference in the lattice mismatch between Cu/Co and Pd/Ni MLs, indi-

cates that their structure is influenced by the superposition and interplay of two contributions: one is the *average (overall) lattice* compositional modulation, and the second is a $\Lambda$*-dependent modulation* that is important for structure modifications and strain effects in the short-$\Lambda$ regime. In Pd/Ni (Cu/Ni) MLs the former is dominant in the long-$\Lambda$ regime, that is above $\sim 10$ ($\sim 15$) atomic planes.[36,39] In the intermediate-$\Lambda$ regime the coherency strains can be balanced by the average lattice effects and may cause a lowering of lattice symmetry (defect) that produces incoherent layer stacking. In Pd/Ni (Cu/Ni) MLs the $\Lambda$ is about 4(9) atomic planes for the intermediate-$\Lambda$ regime.[39,40] Since the layer thicknesses are much shorter than the electron mean-free path, then the induced defects in the intermediate-$\Lambda$ regime may affect the density $N_c$ of free electrons and cause a nonmonotonic dependence of $\omega_p$ with $\Lambda$.[38] In our Co/Cu MLs, that exhibit the same lattice spacing mismatch with the Cu/Ni MLs, the constant $t_{\mathrm{Cu}}$ of 2.1 nm corresponds to $\sim 10$ atomic planes and the long-$\Lambda$ regime is expected to occur for $t_{\mathrm{Co}} \geqslant 1.3$ nm ($\sim 6$ atomic planes), assuming the elasticity properties of the constituents are the same. The observed change in the variation of $\omega_p$, and the other interband parameters in Fig. 8, occurs within the range of $1.3 \leqslant t_{\mathrm{Co}} \leqslant 1.7$ nm that defines an intermediate-$\Lambda$ regime for these Co/Cu MLs. Thus, the developed defects at Co–Cu interfaces, resulting from competition between coherency strains and the average lattice modulation, may alter the overall free-carrier density as a function of $\Lambda$. This is in accordance with reported angle-resolved photoemission spectra,[41] where epitaxially grown ultrathin Cu films on Co(111) exhibited a bulklike continuous dispersion for the $sp$ state, showing that the Cu/Co(111) interface is essentially transparent. The analysis of these spectra[41] shows that the Cu–Co(111) system, unlike the Cu–Co(100) and Cu–Co(110) systems, does not have a significant gap near the Fermi level for electronic confinement.

An explanation is now required for the inverse variation of $\omega_p$ with $\Lambda$, that occurs between the Co/Cu or Ni/Cu and the Ni/Pd MLs. It is well known[42] that for metals the density of states per atom is a universal function of the electron-to-atom ratio within a given structure. As a result the density of states near the Fermi level, $N(E_F)$, exhibits a sequence with alternative maximum and minimum values as a function of the valence electrons per atom, for elements belonging in the same row of the periodic table. This classification scheme shows that Pd exhibits the highest $N(E_F)$ from all the other metals while Cu exhibits the lowest. Consequently, the inverse variation of $\omega_p$ upon $\Lambda$ that is observed in Pd/Ni and Cu/Co MLs can be explained, first, from a large difference in the $N(E_F)$ between the nonmagnetic components (Pd and Cu) and, second, from electronic energy changes near $E_F$ due to hybridization and magnetic polarization effects near the interfaces.

To understand the variation of the interband parameters $E$ and $\gamma$ with $t_{\mathrm{Co}}$, the influence of interface Co atoms in the electronic structure of Cu layers should be considered. The majority and minority spin bands of Co have been mapped out along the (001) direction in Co/Cu MLs by means of photoemission experiments and the observed dispersion of the electronic states was compared to fully relativistic band structure calculations for fcc-Co.[43] To the best of our knowledge, there is not a similar study in the dispersion of electronic states along the (111) direction in Co/Cu MLs and this is an attempt to correlate the observed features in the optical response function $\epsilon(\omega)$ with changes near the $N(E_F)$. In Fig. 6 the positions of the broad interband peaks match with the observed range of optical transitions in the $\epsilon_2(\omega)$ spectra of pure-Cu films. Thus, the obtained variation of $E$ and $\gamma$ parameters with $t_{\mathrm{Co}}$ (Fig. 8) can be attributed to $3d$-spin polarization of Cu induced from a progressive enhancement of Co layer magnetization by increasing $t_{\mathrm{Co}}$. In support of this argument, x-ray magnetic circular dichroism measurements[44] in Co/Cu(111) MLs indicate that the induced Cu moment is primarily situated at the Co/Cu interfaces, which consist of $\sim 2$ atomic layers of Cu, and its average moment is shown to fall off inversely with $t_{\mathrm{Cu}}$. Also, x-ray absorption and x-ray emission spectroscopy[45] of Co and Cu layers in Co/Cu MLs indicate that the $3d$-density of states of Cu interface layers is enhanced near the Fermi level relative to bulk metal. In addition, layer morphology effects induce a random distribution of strain-driven interface defects and create a distribution of exchange-split $d$ levels in $N(E_F)$ of Cu, resulting in the dispersion of photon absorption energies. Such modifications in the optical electronic states may diminish the interband threshold energies of Cu and can be responsible for the smoother decay of the $\epsilon_2(\omega)$ spectra (Fig. 6) with increasing $t_{\mathrm{Co}}$. Thus, the obtained lowering of the energy peak positions and the enhanced peak broadening (Fig. 8) as a function of $t_{\mathrm{Co}}$ (or $\Lambda$) is related to the degree of $s$-$d$ hybridization near the Fermi energy of Cu at the Co/Cu interfaces and the extra contribution from the Co optical electronic states for thicker Co layers. Consequently, the nonmonotonic behavior, observed near the $t_{\mathrm{Co}} \approx 1.3$ nm (Figs. 7 and 8), is indicative for the Co concentration limit where the electronic film density is periodically modified in a different way from the Co/Cu multilayer stacking.

## V. DISCUSSION AND CONCLUSIONS

In this study a series of sputtered Si(100)/$\{\mathrm{SiN}_x(100\ \mathrm{nm})/\{[\mathrm{Co}(t_{\mathrm{Co}})/\mathrm{Cu}(2.1\ \mathrm{nm})]_{30}\mathrm{Co}(t_{\mathrm{Co}})\}_{30}$ MLs have been deposited under specific deposition conditions that gave GMR curves with small hysteresis for $t_{\mathrm{Co}} < 1.3$ nm. The selected film processing is based on the layering modification induced from the intrinsic ($s_{\mathrm{int}}$) and thermal ($s_{\mathrm{th}}$) stresses that are developed between the substrate and the film during deposition. The $s_{\mathrm{int}}$, in general, increases with increased film thickness but also depends on deposition rate and temperature by lattice mismatches between the substrate and the film, lattice defects, and impurities. Thermal stress occurs when the film and the substrate expand and contract at different rates during thermal cycling. Since the XRR measurements do not reveal any bowing effect from tensile or compressive film-substrate stresses, the Co/Cu layer morphology is controlled by strain-driven lattice and interface defects that are gradually developed during deposition. A recent investigation into the effect of deposition conditions on GMR curves of $\{\mathrm{Co}(1\ \mathrm{nm})/\mathrm{Cu}(2.1\ \mathrm{nm})\}_{30}$ MLs[16] indi-

cates that primarily the thermal isolation of the substrate from the supporting copper table together with low sputtering deposition rates create a bimodal distribution of grain sizes with maxima at ~10 and ~21 nm. The achieved microstructure from this deposition process gave GMR curves that are suitable for use in magnetic sensors.[46]

XRR, magnetic, magneto-transport, and SE measurements were used together to examine the alteration of their properties as a function of $t_{Co}$. Notably, the obtained film density and roughness (Fig. 2), the saturation and coercivity fields, the reduced remnant magnetization and GMR ratios (Fig. 4), and the $\epsilon(\omega)$ related parameters exhibit a significant divergence as a function of $t_{Co}$ in the range between 1.3 and 1.6 nm. An extensive discussion of the fitting models has been considered necessary in order to justify the validity of the obtained parameters from the experimental data. Here is presented an attempt to correlate the observed microstructural, magneto-transport, and magnetic *relative* differences, induced by varying $t_{Co}$ in (111) textured Co/Cu MLs, with an alteration of the optical electronic states of Co and Cu at $N(E_F)$. A comparison of the obtained plasma energies $\omega_p$ and interband transition parameters with those reported in Cu/Ni and Pd/Ni MLs[38,39] indicates that their structure is influenced by the superposition and interplay of two contributions: one is the *average (overall) lattice* compositional modulation, and the second is a $\Lambda$-*dependent modulation* that is important for structure modifications and strain effects in the short-$\Lambda$ regime. According to this interpretation, it is possible to understand the common anomaly, observed between $1.3 \leqslant t_{Co} \leqslant 1.7$ nm, in the variation of all the parameters examined here as a function of $t_{Co}$. This is attributed to an intermediate-$\Lambda$ regime where a competition between coherency strains and average lattice modulation may alter the overall free-carrier density and the electronic density of states near the Fermi level $N(E_F)$ as a function of $\Lambda$. Although the optical SE spectra belong to MLs with a complex microstructure, the obtained nonmonotonic variation of $\omega_p$ from $\Lambda$, appearing in a range of $\Lambda$ values where Cu/Ni and Pt/Ni MLs also exhibit a similar anomaly, indicates that this behavior may generally be expected in TM/NM MLs when internal film stresses induce a strain-driven layer growth morphology during deposition. SE measurements on various TM/NM MLs, grown under the specific deposition conditions, are planned for the near future in order to investigate the generality of the $\omega_p$ anomaly at an intermediate-$\Lambda$ regime.

## ACKNOWLEDGMENT

This work has been supported by the EKBAN-280 project of the General Secretariat for Research and Technology of the Development Ministry in Greece.

[1] S. S. P. Parkin, Z. G. Li, and D. J. Smith, Appl. Phys. Lett. **58**, 2710 (1991).
[2] S. S. P. Parkin, Mater. Res. Soc. Symp. Proc. **231**, 211 (1992).
[3] M. J. Hall, B. J. Hickey, M. A. Howson, M. J. Walker, J. Xu, D. Greig, and N. Wiser, Phys. Rev. B **47**, 12 785 (1993).
[4] W. F. Egelhoff, Jr., P. J. Chen, C. J. Powell, M. K. Stiles, and R. D. McMichael, J. Appl. Phys. **79**, 2491 (1996).
[5] W. F. Egelhoff, Jr., and M. T. Kief, Phys. Rev. B **45**, 7795 (1992).
[6] R. Coehoorn, M. T. Johnson, W. Folkerts, S. T. Purcell, N. W. E. McGee, A. De Veirman, and P. J. H. Bloemen, in *Magnetism and Structure in Systems of Reduced Dimension*, NATO ASI Series B. Physics, Vol. 309, edited by R. F. C. Farrow, B. Dienny, M. Donath, A. Fert, and B. D. Hermsmeier (Plenum, New York, 1993), p. 295.
[7] *Ultrathin Magnetic Structures II*, edited by B. Heinrich and J. A. C. Bland (Springer, Berlin, 1994), Chap. 2.
[8] S. S. P. Parkin, R. Bhadra, and K. P. Roche, Phys. Rev. Lett. **66**, 2152 (1991).
[9] S. S. P. Parkin, R. F. C. Farrow, R. F. Marks, A. Cebollada, G. R. Harp, and R. J. Savoy, Phys. Rev. Lett. **72**, 3718 (1994).
[10] S. Logothetidis, J. Petalas, N. K. Flevaris, and R. L. Johnson, Thin Solid Films **234**, 538 (1993).
[11] S. Uba, L. Uba, A. Ya Perlov, A. N. Yaresko, V. N. Antonov, and R. Gontarz, J. Phys.: Condens. Matter **9**, 447 (1997) and references therein.
[12] L. Neel, Comp. Rend. Acad. Sci. (France) **255**, 1545 (1962); L. Neel, *ibid.* **255**, 1676 (1962).
[13] D. J. Kubinski and H. Holloway, J. Appl. Phys. **79**, 1661 (1996).
[14] W. F. Egelhoff, Jr., P. J. Chen, C. J. Powell, M. D. Stiles, and R. D. McMichael, J. Appl. Phys. **79**, 2491 (1996).
[15] W. F. Egelhoff, Jr., P. J. Chen, C. J. Powell, M. D. Stiles, R. D. McMichael, C.-L. Lin, J. M. Sinertsen, J. H. Judy, K. Takano, and A. E. Berkowitz, J. Appl. Phys. **80**, 5183 (1996).
[16] C. Christides, S. Stavroyiannis, N. Boukos, A. Travlos, and D. Niarchos, J. Appl. Phys. **83**, 3724 (1998).
[17] L. Vina, S. Logothetidis, and M. Cardona, Phys. Rev. B **30**, 1979 (1984).
[18] F. Bridou, J. Phys. III **4**, 1513 (1994).
[19] H. Holloway and D. J. Kubinski, J. Magn. Magn. Mater. **170**, 95 (1997).
[20] T. P. Russel, Mater. Sci. Rep. **5**, 171 (1990).
[21] A. P. Payne and B. M. Clemens, Phys. Rev. B **47**, 2289 (1993).
[22] D. K. G. de Boer, A. J. G. Leenaers, and W. W. van de Hoogenholf, J. Phys. III **4**, 1559 (1994).
[23] L. Nevot and P. Croce, Rev. Phys. Appl. **15**, 761 (1980); **11**, 113 (1976).
[24] T. J. Minvielle, R. J. Wilson, and R. L. White, Appl. Phys. Lett. **68**, 2750 (1996).
[25] R. Castaner, C. Prietro, A. de Andres, J. L. Martinez, J. Trigo, and J. M. Sanz, Solid State Commun. **98**, 179 (1996).
[26] A. M. Shukh, D. H. Shin, and H. Hoffmann, J. Appl. Phys. **76**, 6507 (1994).
[27] F. J. A. den Broeder, W. Hoving, and P. J. H. Bloemen, J. Magn. Magn. Mater. **93**, 562 (1991).
[28] C. H. Lee, H. He, F. J. Lamelas, W. Vavra, C. Uher, and R. Clarke, Phys. Rev. B **42**, 1066 (1990).
[29] J. Kohlhepp, H. J. Elmers, and U. Gradmann, J. Magn. Magn. Mater. **121**, 487 (1993).
[30] (a) R. J. Highmore, W. C. Shih, R. E. Somech, and J. E. Evetts, J. Magn. Magn. Mater. **116**, 249 (1992); (b) Z. J. Yang and M. R. Scheinfein, Phys. Rev. B **52**, 4263 (1995); (c) M. J. Hall, E. D. Whitton, D. B. Jardine, R. E. Somech, J. E. Evetts, and J. A. Leake, Thin Solid Films **275**, 195 (1996); (d) E. E. Fullerton, M. J. Conover, J. E. Mattson, C. H. Showers, and S. D. Bader, Phys. Rev. B **48**, 15 755 (1993).
[31] D. A. Thompson, L. T. Romankiw, and A. F. Maydas, IEEE Trans. Magn. **MAG-11**, 1039 (1975).
[32] T. Eckl, G. Reiss, H. Bruckl, and H. Hoffmann, J. Appl. Phys. **75**, 362 (1994).
[33] M. Cardona, in *Modulation Spectroscopy*, Suppl. 11 of Solid State Physics, edited by F. Seitz, D. Turnbull, and H. Ehrenreich (Academic, 1969).
[34] R. Lässer, N. V. Smith, and R. L. Benbow, Phys. Rev. B **24**, 1895 (1981).
[35] A. Y.-C. Yu, T. M. Donovan, and W. E. Spicer, Phys. Rev. **167**, 670 (1968).
[36] A. Y.-C. Yu and W. E. Spicer, Phys. Rev. **167**, 674 (1968).
[37] U. Gerhardt, D. Beaglehole, and R. Sandrock, Phys. Rev. Lett. **19**, 309 (1967).
[38] S. Logothetidis and N. K. Flevaris, J. Appl. Phys. **75**, 7978 (1994).
[39] N. K. Flevaris, in Ref. 6, p. 425.
[40] T. Tsakalakos and J. E. Hilliard, J. Appl. Phys. **54**, 734 (1983).
[41] E. D. Hansen, T. Miller, and T.-C. Chiang, J. Phys.: Condens. Matter **9**, L435 (1997).
[42] W. A. Harrison, in *Electronic Structure and the Properties of Solids* (Freeman, San Francisco, 1980), Chap. 20.
[43] C. M. Schneider, A. K. Schmid, P. Schuster, H. P. Oepen, and J. Kirschner, in Ref. 6, p. 453.

[44] G. A. Held, M. G. Samant, J. Stohr, S. S. P. Parkin, B. D. Hermsmeier, M. van Schilfgaarde, and R. Nakajima, Z. Phys. B **100**, 335 (1996).
[45] A. Nilsson, J. Stohr, T. Wiell, M. Alden, P. Bennich, N. Wassdahl, M. G. Samant, S. S. P. Parkin, N. Martensson, J. Nordgren, B. Johansson, and H. L. Skriver, Phys. Rev. B **54**, 2917 (1996).
[46] C. Christides, S. Stavroyiannis, G. Kallias, A. Nasiopoulou, and D. Niarchos, to be presented in Eurosensors XII conference, Southampton, England, September 1998.